eprints@whiterose.ac.uk
https://eprints.whiterose.ac.uk/

Complexities of atomic structure at CdO/MgO and CdO/Al $_2$O $_3$ interfaces

Everett D. Grimley, Alex P. Wynn, Kyle P. Kelley [iD], Edward Sachet [iD], Julian S. Dean, Colin L. Freeman [iD], Jon-Paul Maria, and James M. LeBeau

View Online   Export Citation   CrossMark

ARTICLES YOU MAY BE INTERESTED IN

Complexities of atomic structure at CdO/MgO and CdO/Al$_2$O$_3$ interfaces

Everett D. Grimley,[1,a)] Alex P. Wynn,[2] Kyle P. Kelley,[1] Edward Sachet,[1] Julian S. Dean,[2] Colin L. Freeman,[2] Jon-Paul Maria,[3] and James M. LeBeau[1,b)]

[1]*Department of Materials Science and Engineering, North Carolina State University, Raleigh, North Carolina 27606, USA*
[2]*Department of Materials Science and Engineering, University of Sheffield, Sheffield S1 3JD, United Kingdom*
[3]*Department of Materials Science and Engineering, Pennsylvania State University, State College, Pennsylvania 16802, USA*

We report the interface structures of CdO thin films on (001)-MgO and (0001)-Al$_2$O$_3$ substrates. Using aberration corrected scanning transmission electron microscopy, we show that epitaxial growth of (001)-CdO‖(001)-MgO occurs with a lattice misfit greater than 10%. A high density of interface misfit dislocations is found to form. In combination with molecular dynamics simulations, we show that dislocation strain fields form and overlap in very thin heterostructures of CdO and MgO (< 3 nm). On the *c*-Al$_2$O$_3$ substrate, we find that CdO grows with a surface normal of [025]. We show that three rotation variants form due to the symmetry of the sapphire surface. These results contribute insights into the epitaxial growth of these rock-salt oxides. *Published by AIP Publishing.*
https://doi.org/10.1063/1.5053752

I. INTRODUCTION

Recently, it has been demonstrated that cation doping can substantially increase carrier mobility and conductivity of CdO thin films.[1–9] High carrier mobility and *n*-type conductivity have been obtained for intrinsic and doped films on both (0001)-Al$_2$O$_3$ and (001)-MgO substrates. In certain instances, the mobility and conductivity of these films can rival, and even surpass, those of many conventional transparent oxide conductors like indium tin oxide[10] and ZnO.[11] These remarkable properties have thus made CdO of interest for plasmonic applications.[1,3,5,8,9]

CdO adopts the rock-salt structure and can readily be grown on rock-salt MgO.[1,5] A variety of growth methods can be used to prepare CdO epitaxial films including pulsed DC and RF power reactive co-sputtering,[8] pulsed laser deposition,[1] chemical solution deposition,[3] and molecular beam epitaxy.[5] On MgO-(001), CdO grows (001)-oriented despite its lattice parameter ($a = 4.70$ Å) being $\sim 11.5\%$ larger than MgO ($a = 4.21$ Å).[1,5] This significant mismatch leads to the formation of misfit dislocations at interfaces with strain fields that extend into the thin film. Quantitative characterization of dislocations and strain is thus needed as electronic properties can be modified influenced by their presence.

The growth of CdO on non-rock-salt substrates has also been investigated as it can be difficult to control the MgO surface quality and structural integrity.[12] Instead, *c*-Al$_2$O$_3$ has proven a robust growth surface for CdO films[2,8] where the mobilities and carrier densities are comparable to those of films grown on MgO.[8,9] This finding is unexpected given that the cubic rock-salt CdO differs substantially in symmetry from the corundum structure, which might be expected to lead to poor quality growth. It has been found, for example,

that CdO grows (025)-oriented on *c*-Al$_2$O$_3$ with three identical in-plane rotational variants.[2,8] The precise origin of the rotation variants and the interface structure, however, warrants further investigation to gain further control over the electronic properties.

In this article, we utilize scanning transmission electron microscopy (STEM) to characterize CdO films grown on MgO and Al$_2$O$_3$ substrates. On MgO, the generation of misfit dislocations and overlapping strain fields is revealed. Molecular dynamics simulations are used to gain further insights into stress field interactions. Turning to *c*-Al$_2$O$_3$ substrates, we resolve the precise arrangement atom columns at the interface and construct a 3D model to understand the precise origins of the rotation variants. For both substrates, we demonstrate that high quality epitaxial growth occurs despite either the substantial lattice or symmetry mismatch.

II. MATERIALS AND METHODS

A. Thin film growth

CdO films were grown on (001)-oriented MgO substrates with oxide molecular beam epitaxy as described in Ref. 5. The CdO films were approximately 1, 1.7, 3, 5.5, and 9 nm and capped with ~ 12 nm of MgO. Cross sections were prepared for STEM using a focused ion beam (FEI Quanta 3D FEG) with final thinning at 2 kV. Uncapped, 100 nm CdO films were grown on *c*-Al2O$_3$ substrates with reactive DC magnetron sputtering as in Ref. 8. Samples for electron microscopy were then prepared via mechanical wedge polishing (Allied High Tech Multiprep) and Ar ion milling (Fischione Model 1050) with liquid nitrogen cooling.

B. Electron microscopy

Annular dark-field (ADF) STEM was performed on a probe-corrected FEI Titan G2 60-300 kV operated at 200 kV.

a)Electronic mail: edgrimle@ncsu.edu
b)Electronic mail: jmlebeau@ncsu.edu

Beam currents between 30 and 60 pA were used. The probe convergence semi-angle was 19.6 mrad, and the ADF detector inner semi-angle was 34 and 28 mrad for CdO‖MgO and CdO‖c-Al$_2$O$_3$, respectively. Low-angle ADF (LAADF) detector inner semi-angles were used for imaging to increase the sensitivity to defects and strain.[13] LAADF additionally enables better simultaneous visualization of the heavy Cd and light Mg/O atoms.

The RevSTEM method was employed to minimize drift induced image distortion,[14] using twenty to forty 1024 × 1024 frames and a 2 µs/pixel dwell time. Local strain was measured using geometric phase analysis (GPA) performed using the FRWRtools plugin.[15]

C. Molecular dynamics

Molecular dynamics simulations were performed to examine the stresses in CdO/MgO heterostructures. The potentials for MgO and CdO were taken from Ref. 16, and all crystal structures were optimized in GULP[17] prior to carrying out molecular dynamics simulations. The MgO and CdO slabs were generated by cleaving the periodic crystals to produce two (001) surfaces. The CdO film layers for five different thicknesses were then sandwiched between MgO periodic slabs. All molecular dynamics simulations were performed using a modified version of DL_POLY Classic,[18,19] which calculates the atomic virial information directly.

The simulations were performed in the NVT canonical ensemble with a Nosé-Hoover thermostat (relaxation time 10 fs). Each interface was relaxed for 1 ns at 10 K to identify any issues with the initial placement of the block. A longer equilibration was then performed at 300 K. After equilibration, virial data were collected from 2 ns production runs. All simulations used a time step of 1 fs. The outermost layers of the MgO slabs were kept frozen during the simulations to ensure the MgO maintained bulk characteristics.

D. Virial stress analysis

Stresses obtained from molecular dynamics simulations were expanded to larger length scale by the virial method. From the atomistic system of volume, Ω, the local atomic-level stress field, $\Pi^{\alpha\beta}$, was calculated through volumetric averaging over the constituent atomic virials, W:

$$\Pi^{\alpha\beta} = \frac{1}{\Omega} \sum_i W_i^{\alpha\beta}, \tag{1}$$

where for the two-body interatomic potentials, $\phi_{ij}(r)$. The ith atomic virial is then:

$$W_i^{\alpha\beta} = -m_i v_i^\alpha v_i^\beta - \frac{1}{2} \sum_{j \neq i} \left(\frac{-1}{r_{ij}} \frac{-\partial \phi_{ij}(r_{ij})}{\partial r} \right) r_{ij}^\alpha r_{ij}^\beta + \cdots . \tag{2}$$

Here, α and β indicate directions in an orthogonal laboratory frame. The position and velocity of atom i are r_i and v_i, respectively, while r_{ij} is the separation between atoms i and j. The ellipsis denotes additional higher order contributions to the virial stress tensor that are present within the atomistic simulations.

At all points in time, the virial stress can be broken down into three components: the physically meaningful Cauchy stress tensor, the contribution from random thermal fluctuations, and a mathematical artifact caused by the lack of symmetry in multi-component systems (such as the ionic structures considered here). The thermal fluctuations were removed by averaging the virial stress over time. The mathematical artifact was removed by averaging the contribution of each atom over a volume using a weighting function given by

$$\Pi^{\alpha\beta}(r) = \sum_i \psi(r - \langle r_i \rangle) \left\langle W_i^{\alpha\beta} \right\rangle, \tag{3}$$

where i is defined as the atoms within a cutoff distance from point r, and $\psi(r)$ is a 7th order polynomial Hardy function,[20]

$$\psi(r) = (1 - r^2)^2 \left[\frac{1}{2} - \frac{3}{2}\left(r - \frac{1}{2}\right) + 2\left(r - \frac{1}{2}\right)^3 \right]. \tag{4}$$

Though the exact form of the localization function was not
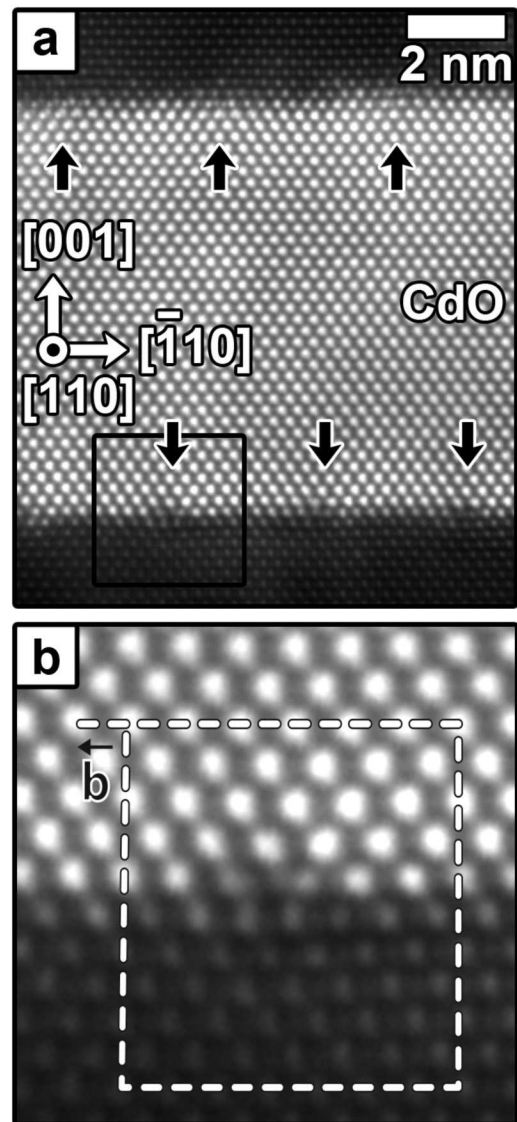

FIG. 1. (a) LAADF STEM image of the 5.5 nm thick CdO film interface viewed down the [110] zone-axis with the location of edge dislocations indicated by black arrows) at the CdO‖MgO interfaces. (b) Expanded view of the rectangular inset in (a) with Burgers circuit indicating that the misfit **b**'s are of type $\langle 110 \rangle/2$.

crucial, it does impact on how smooth the stress field convergence is overall. The Hardy function was found to yield smooth convergence of stress fields with a larger cutoff distance, while significantly reducing the computational cost compared to Gaussian distribution functions.

III. RESULTS AND DISCUSSION

A. Epitaxial growth of CdO on (001) MgO

When viewed along $\langle 110 \rangle$ as in Fig. 1(a), the MgO∥CdO thin films are found to be fairly abrupt with the formation of a periodic array of misfit dislocations (black arrows) at the top and bottom interfaces. These misfit dislocations form during relaxation of epitaxial growth of films on lattice misfit substrates.[21,22] As shown in Fig. 1(b), two additional $\{\bar{2}20\}$-MgO planes are found at the dislocation core. Based on the Burgers circuit, the Burgers vectors are of type $\langle 110 \rangle/2$. The dislocation lines, ξ, lie along both $\langle 110 \rangle$ in the (001) interfacial plane, i.e., $\xi_1 = [110]$ and $\xi_2 = [\bar{1}10]$. As such, the dislocations are perfect edge dislocations.

The identified dislocations are consistent with those found at other rock-salt/rock-salt interfaces. For example, dislocation networks have been identified in PbTe∥PbSe rock-salts with ∼7% misfit.[23,24] Moreover, similar $\langle 110 \rangle$-type dislocations with orthogonal $\langle 110 \rangle$-type Burgers vectors have been seen in the interfacial plane of TiN-(001)∥NbN-(001) metal-like rock-salt nitride systems with ∼ 3.6% misfit.[25]

Highly mismatched systems grow to minimize misfit by balancing (1) epitaxial strain absorbed by the lattice and (2) strain accommodated by the formation of misfit dislocations.[21,22] For the CdO and MgO interface, the greatest

lattice coincidence occurs when the equation

$$d_{\{110\}\text{CdO}} \times N_{\text{CdO}} \approx d_{\{110\}\text{MgO}} \times (N+1)_{\text{MgO}} \qquad (5)$$

is approximately satisfied, i.e., when N repeat units of unstrained CdO occupy nearly the same interfacial area as $N+1$ repeat units of unstrained MgO based on their respective $\{110\}$ interplanar spacings d. At certain integer values that satisfy this equation, a misfit dislocation forms to accommodate an extra set of $\{110\}$ MgO planes.

Solutions to this equation occur for $N = 9$ or 10. The length across 9 unstrained CdO $\{110\}$ planes is 12 pm smaller than 10 MgO $\{110\}$ planes. Similarly, the distance across 10 CdO $\{110\}$ is 20 pm larger than 11 MgO planes. Based on the interplanar spacings, misfit dislocations would thus be expected to lie between 3.0 nm and 3.3 nm apart to minimize strain. The dislocation spacings measured from experiment were on average ∼3.25 nm for the 1 nm and 5.5 nm thick films, which is in good agreement with the calculated range. Furthermore, as the dislocation separation is found to be independent of thickness, the CdO films are already relaxed for a film even 1 nm thick.

Strain within the CdO layers is further investigated by geometric phase analysis (GPA).[26] The in-plane ϵ_{xx} and out-of-plane ϵ_{yy} strain components with respect to a reference region of MgO are shown in Fig. 2. The strain within the MgO substrate and cap is ∼ 0.0%, indicating a suitably selected reference region in each instance. As expected from the mismatch of the film and substrate, GPA finds the CdO film regions to be ∼ 10% larger than the MgO. Furthermore, the ϵ_{xx} in-plane strain in Fig. 2 indicates that the MgO is under compression near the dislocation cores while under
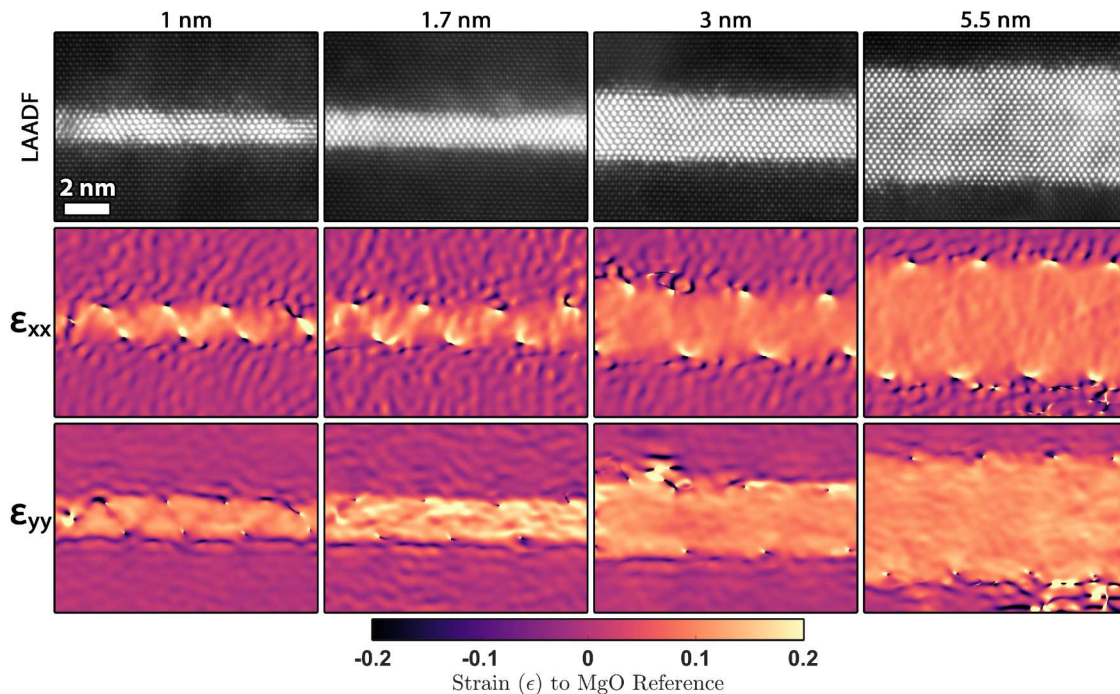

FIG. 2. LAADF STEM images of ∼1, 1.7, 3, and 5.5 nm CdO∥MgO heterostructures viewed down the [110] zone axis. ϵ_{xx} and ϵ_{yy} derived from geometric phase analysis of the 002/111 reflections using the MgO as a reference reveal the strains near the dislocation cores, as well as zigzagging strain fields in the thinner films that originate from overlap of dislocation stress fields. The color scale range is set to enhance visualization of the dislocation strain fields.

tension in CdO. In contrast, the ϵ_{yy} components are more localized to the vicinity of the dislocation cores.

The LAADF STEM images also reveal differences in the CdO thin films with increasing thickness. As seen in the LAADF STEM in Fig. 2, the thinner films—1 nm and 1.7 nm—possess regions with dark contrast and distorted atom columns on (111) as seen in the figure. These contrast variations are not clearly present in thicker films.

Careful investigation of the GPA strain measurements further reveals key differences as a function of thickness. The thinner film (1 nm and 1.7 nm) strain distributions show non-uniformity near the center of the CdO film. Specifically, a zig-zagging pattern of strain occurs between the dislocations across the film. Along the zigzag, CdO expands in-plane (ϵ_{xx}) and compresses out-of-plane (ϵ_{yy}). In contrast to the thinner films, increasing CdO thickness reduces this behavior and is no longer strongly present for confined films ~3-5.5 nm thick.

The zigzagging strain field likely originates due to the overlap of the dislocation strain fields between the two interfaces. Because the regions of the highest lattice distortion are confined to the relatively close proximity of the dislocations, the strain field network formation disappears when transverse dislocations are spaced such that highly strained regions no longer overlap.

Strain behavior was further evaluated using molecular dynamics simulations for CdO films and CdO/MgO hetero-structures. From the simulations, large distortions are imme-diately apparent at the MgO-CdO interface along both [110] and [$\bar{1}$10] in the plane of the interface, which is in good agreement with the experiment (see Fig. 3). The simulation results can be evaluated quantitatively by applying the virial algorithm along $\langle 110 \rangle$ as described above to generate the 6 stress terms for each atom. The average of the normal, σ_{xx}, and shear, σ_{xy}, stress for all the Cd and O atoms across the 5.5 nm CdO layer is shown in Figs. 3(c) and 3(d), respec-tively. The σ_{xx} ranges between +1.5 GPa and −1.5 GPa, indicating that there are regions of tension and compression. The majority of the atoms, however, are under a compressive stress as would be expected from the larger lattice parameter of the CdO compared to the MgO.

The shear stresses are approximately half that (+0.8 GPa to −0.8 GPa) of the normal stresses. However, the shear stresses show a clearer periodic pattern acting in a clockwise and anti-clockwise motion. Figure 3(e) shows the shear term for the first layer of Cd and O atoms in the structure (i.e., those in direct contact with Mg), while Fig. 3(f) shows a layer of CdO from the middle of slab and which shows that the absolute stresses decrease away from the surface.

The stress periodicity is ~2.5 nm for all thicknesses of confined CdO slabs simulated. While this is ~0.75 nm smaller than the dislocation spacing measured from experi-ment, some small differences are expected and may relate to the relaxation of the boundary conditions in the simulations that allow for some stress relaxation. Furthermore, the stress periodicity from molecular dynamics is found to be indepen-dent of the thickness of the confined CdO slab.

For a 1 nm confined film model, the CdO system is completely saturated by the influence of the two interfaces because the stress penetrates across the entire CdO slab and
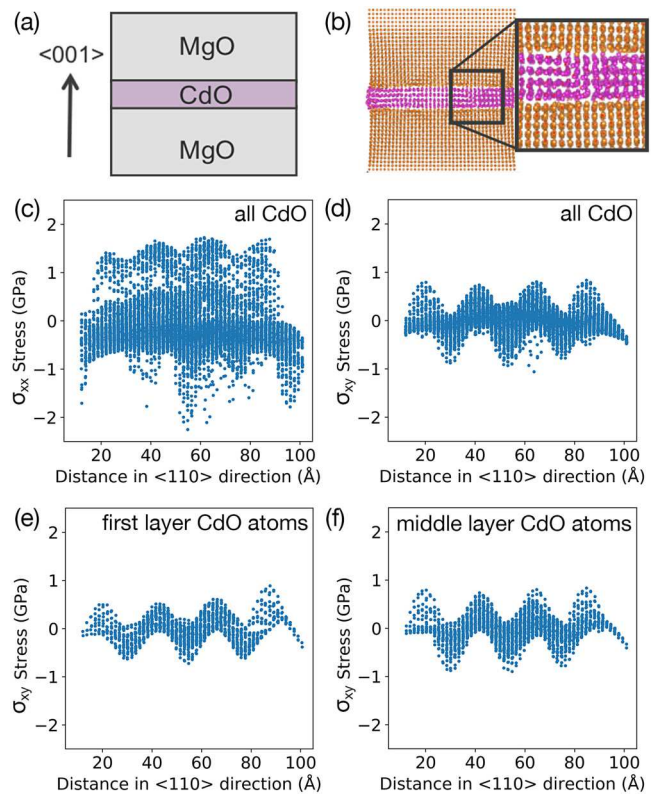

FIG. 3. (a) and (b) Molecular dynamics simulation of a 3 nm CdO thick layer with the inset showing a high strain region consistent with a dislocation. (c) and (d) show the stress maps for all the CdO atoms in the 3 nm slab along $\langle 110 \rangle$, while (e) and (f) show stress only for atoms in the first and middle layers, respectively. Stress periodicity is weak for *sigma*$_{xx}$ and strong for σ_{xy}.

no ions are able to relax to a bulk-like structure. As the CdO layer increases in thickness to 3 nm [Fig. 4(a)] the model relaxes at the center, but interfaces still dominate the stress. This is consistent with the diminishing internal strain fields observed in experiment for the 3 nm confined CdO film com-pared to the thinner CdO films.

To further examine the diminishing of stress away from the interfaces, a separate single interface (i.e., a normal thin film‖substrate geometry) was generated between MgO and CdO as shown in Fig. 4(b). For the unconfined CdO thin film, the stress decays to bulk-like values approximately 3-4 nm from the interface. This high stressed state within the first few atomic layers is also consistent with a gradual decay in the overlapping fields observed in the STEM strain analysis.
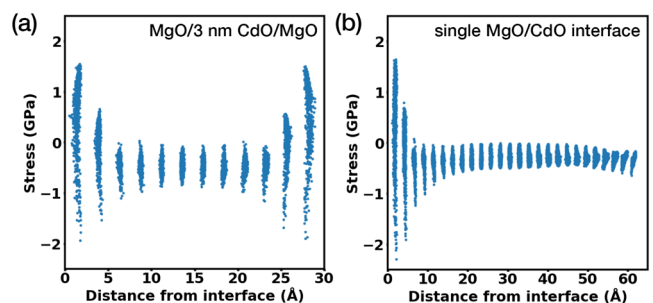

FIG. 4. The influence of stress at the interface for (a) a 3 nm thick CdO layer and (b) a single layer of MgO/CdO to highlight the influence of the interface.

Experiment and simulation thus indicate that the growth of highly misfit rock-salt CdO on the (001) MgO is facilitated by lattice strain and a periodic array of edge dislocations with lines and Burgers vectors of ⟨110⟩-type that lie in the interfacial plane. The out-of-plane ϵ_{yy} strain is fairly localized to the core vicinity, but the in-plane ϵ_{xx} persists further into the CdO film. For the thinnest confined CdO layers, the overlap of the strain fields of the dislocations on opposite interfaces leads to zig-zagging regions of CdO with tension in the ϵ_{xx} and compression in the ϵ_{yy}. These zigzagging regions disappear as film thicknesses increase.

B. Epitaxial growth of CdO on c-Al₂O₃

The interface structure of CdO on sapphire also offers considerable complexities. In spite of the large difference between the cubic rock-salt structure and that of the hexagonal sapphire, the CdO grows with large lateral grain sizes as seen in Fig. 5(a). This is likely the origin of CdO/*c*-Al₂O₃ carrier mobility and conductivity being comparable to CdO films grown on MgO.[5] Analysis of the CdO structure in the LAADF STEM images reveals that the CdO rock-salt structure tilts such that the [052] aligns to the Al₂O₃-[00.1], consistent with X-ray results.[2]

Based on LAADF STEM observations [Fig. 5(a)], the interface plane of CdO is corrugated in its termination on *c*-plane sapphire. This leads to a periodic variation in the interface structure where Cd/O atom columns are present between some of the terminal Al atoms on the sapphire and absent between others. In addition, the shape and intensity of the atom columns vary at the interface. Brighter atom columns exist, for example, suggesting greater Cd occupancy and/or increased structural uniformity along the depth of those columns. Other columns are dim, blurry, and even distorted into oval shapes, indicating an increase in displacements along an atom column. Visual inspection of the CdO structure near the interface shows that the CdO on *c*-Al₂O₃ does not form periodic misfit dislocations, in contrast to CdO on MgO. Also, the observed structure exhibits little-to-no structural distortion except for the first layer of Cd atoms columns.

A boundary between two [052] rotation variants is shown in Fig. 5(b). The boundary forms between a grain aligned along [100] on the left and a 120° rotation variant on the right. Inspection of the interface structure in the region shows that the boundary did not form at a substrate flaw or
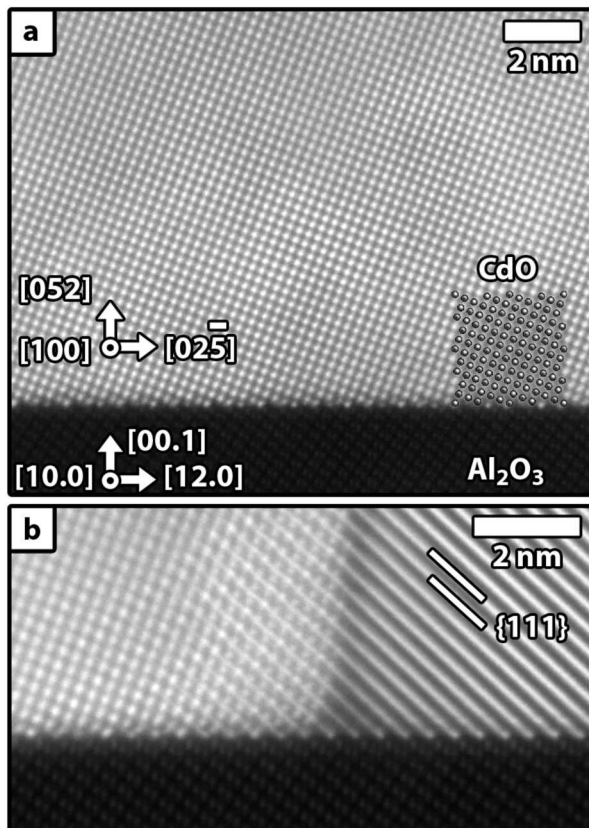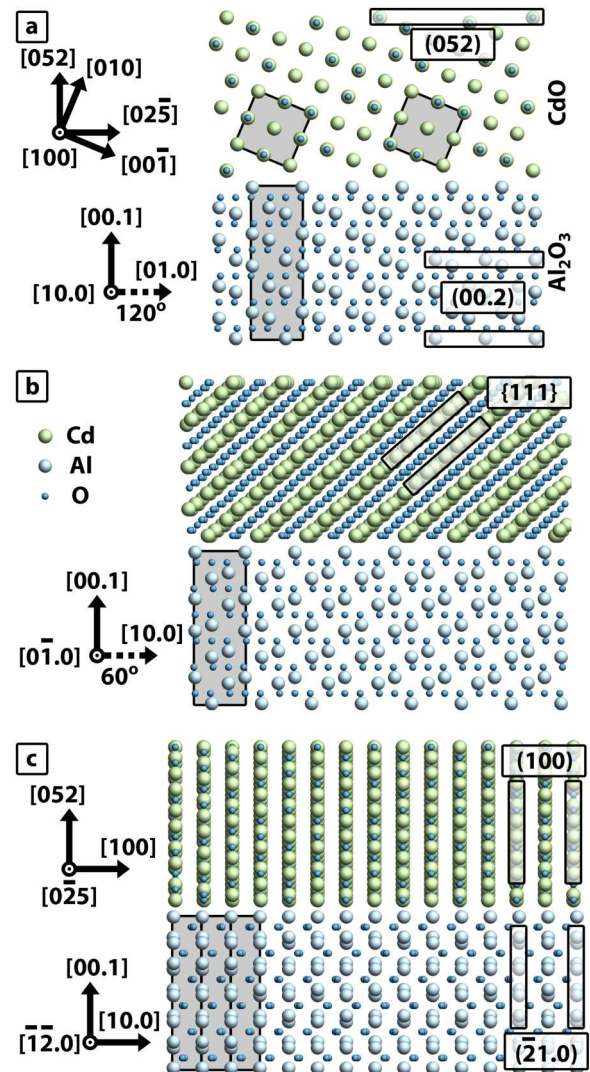

FIG. 5. LAADF STEM of CdO grown on *c*-Al₂O₃. (a) A region exemplifying how large areas of the film can exhibit high quality epitaxial interfaces and film structures. (b) A boundary between two separate in-plane rotational variants.

FIG. 6. (a)–(c) Schematic representations of the film and interface structures of (052)-CdO‖(00.1)-Al₂O₃, where a single rotational variant is displayed from three relevant projections based on the experiment. Dark shaded regions indicate projection of the unit cells, while light shaded regions indicate relevant planes.
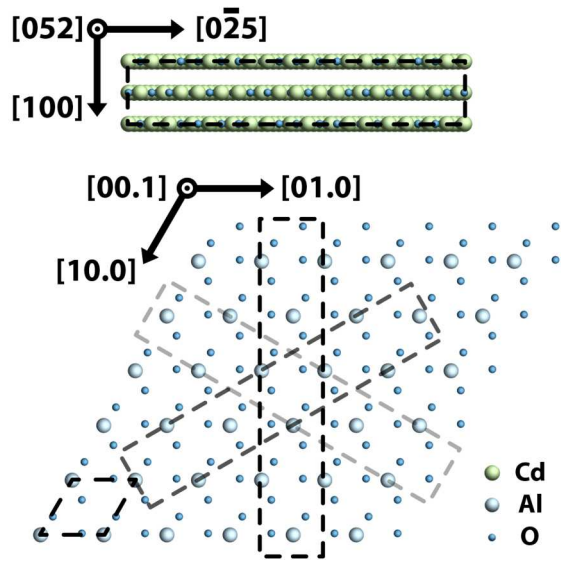
FIG. 7. Schematic of the terminal O and Al layers at the CdO/*c*-Al₂O₃ interface where the hexagonal repeat unit is shown at the bottom left. The CdO-(052) repeat (rectangular dashed overlays) can interface with the surface with (200)//[100] of the CdO aligning with *c*-Al₂O₃ ($\bar{2}$1.0)//[10.0] (light gray), (11.0)//[11.0]/$\sqrt{2}$ (dark gray), and (1$\bar{2}$.0)//[01.0] (black).

step, as has been seen to occur in MgO films on GaN.[27] Instead, the boundaries originate due to nucleation and growth of separate grains that coalesce during growth.

Schematics of the film/interface structures are shown in Fig. 6. Without relaxing the model, the atom positions of the interface and films reproduce the configurations viewed along different zones. The distorted atom column shapes and variation in column intensity from experiment, however, suggests that some relaxation occurs in the CdO structure directly at the interface to facilitate growth. It is important to note, however, that while this model describes the growth orientation of CdO on *c*-Al₂O₃, it is in stark contrast to other (smaller) rock-salt materials on *c*-Al₂O₃ that grow [111]-oriented (e.g., HfN $a = 4.54$ Å, MgO $a = 4.21$ Å, and CrN $a = 4.15$ Å).[28–30]

Based on the experiment and model, the three in-plane rotational variants can be understood in the context of the sixfold symmetry of the sapphire surface. This is shown schematically from a top-down view in Fig. 7. The [100] of CdO can align to [10.0] of Al₂O₃, [11.0]/$\sqrt{2}$, or [01.0] with identical misfit of the (200)-CdO planes to the respective Al₂O₃-($\bar{2}$1.0), (11.0), or (1$\bar{2}$.0) planes. These three different CdO orientations are shown, respectively, as the light gray, dark gray, and black dashed rectangular overlays on the final O and Al layers of Al-terminated *c*-Al₂O₃ in Fig. 7.

IV. CONCLUSIONS

As revealed for CdO thin films on (001)-MgO and (00.1)-Al₂O₃, high quality crystal growth is achievable on both substrates. For CdO films on MgO, dislocation networks form at interface planes, and as film thickness decreases, the strain fields of misfit dislocations begin to overlap and to form strain field networks that zig-zag through the film. For CdO on *c*-Al₂O₃, the lateral grain size in the CdO on

c-Al₂O₃ is limited by the coalescence of rotation variant islands that nucleate and grow with a different in-plane orientation, which is manifest as high-angle grain boundaries formed within the film. These rotation variants form as the [100]-CdO can align to the [10.0], [11.0], or [01.0] directions of *c*-Al₂O₃ with identical misfit. The resulting interface adapts to the difference in symmetry of the substrate by distortion of some of the atom sites in the first plane and changes in site occupancy. Given the considerable structural differences between these interfaces, future work is needed to fully connect misfit and defects to carrier mobility and conductivity for this promising plasmonic material system.

[1] M. Yan, M. Lane, C. R. Kannewurf, and R. P. H. Chang, Appl. Phys. Lett. **78**, 2342 (2001).
[2] J. Zúñiga-Pérez, C. Martínez-Tomás, and V. Muñoz-Sanjosé, Phys. Status Solidi C **2**, 1233 (2005).
[3] R. Maity and K. K. Chattopadhyay, Sol. Energy Mater. Sol. Cells **90**, 597 (2006).
[4] M. Burbano, D. O. Scanlon, and G. W. Watson, J. Am. Chem. Soc. **133**, 15065 (2011).
[5] E. Sachet, C. T. Shelton, J. S. Harris, B. E. Gaddy, D. L. Irving, S. Curtarolo, B. F. Donovan, P. E. Hopkins, P. A. Sharma, A. L. Sharma, J. Ihlefeld, S. Franzen, and J.-P. Maria, Nat. Mater. **14**, 414 (2015).
[6] B. F. Donovan, E. Sachet, J.-P. Maria, and P. E. Hopkins, Appl. Phys. Lett. **108**, 021901 (2016).
[7] Y. Yang, K. Kelley, E. Sachet, S. Campione, T. S. Luk, J.-P. Maria, M. B. Sinclair, and I. Brener, Nat. Photonics **11**, 390 (2017).
[8] K. P. Kelley, E. Sachet, C. T. Shelton, and J.-P. Maria, APL Mater. **5**, 076105 (2017).
[9] E. L. Runnerstrom, K. P. Kelley, E. Sachet, C. T. Shelton, and J.-P. Maria, ACS Photonics **4**, 1885 (2017).
[10] H. Kim, C. M. Gilmore, A. Piqué, J. S. Horwitz, H. Mattoussi, H. Murata, Z. H. Kafafi, and D. B. Chrisey, J. Appl. Phys. **86**, 6451 (1999).
[11] E. Sachet, M. D. Losego, J. Guske, S. Franzen, and J.-P. Maria, Appl. Phys. Lett. **102**, 051111 (2013).
[12] B. E. Gaddy, E. A. Paisley, J.-P. Maria, and D. L. Irving, Phys. Rev. B **90**, 125403 (2014).
[13] D. A. Muller, N. Nakagawa, A. Ohtomo, J. L. Grazul, and H. Y. Hwang, Nature **430**, 657 (2004).
[14] X. Sang and J. M. LeBeau, Ultramicroscopy **138**, 28 (2014).
[15] C. T. Koch, "Determination of core structure periodicity and point defect density along dislocations," Ph.D. thesis (Arizona State University, 2002).
[16] G. V. Lewis and C. R. A. Catlow, J. Phys. C Solid State Phys. **18**, 1149 (1985).
[17] J. D. Gale and A. L. Rohl, Mol. Simul. **29**, 291 (2003).

[18]I. T. Todorov, W. Smith, K. Trachenko, and M. T. Dove, J. Mater. Chem. **16**, 1911 (2006).

[19]R. Darkins, M. L. Sushko, J. Liu, and D. M. Duffy, Phys. Chem. Chem. Phys. **16**, 9441 (2014).

[20]P. S. Branicio and D. J. Srolovitz, J. Comput. Phys. **228**, 8467 (2009).

[21]J. W. Matthews and A. E. Blakeslee, J. Cryst. Growth **27**, 118 (1974).

[22]R. Hull and J. C. Bean, Crit. Rev. Solid State Mater. Sci. **17**, 507 (1992).

[23]G. Springholz and K. Wiesauer, Phys. Rev. Lett. **88**, 015507 (2001).

[24]E. Wintersberger, N. Hrauda, D. Kriegner, M. Keplinger, G. Springholz, J. Stangl, G. Bauer, J. Oswald, T. Belytschko, C. Deiter, F. Bertram, and O. H. Seeck, Appl. Phys. Lett. **96**, 131905 (2010).

[25]L. Hultman, M. Shinn, P. B. Mirkarimi, and S. A. Barnett, J. Cryst. Growth **135**, 309 (1994).

[26]M. J. Hÿtch, E. Snoeck, and R. Kilaas, Ultramicroscopy **74**, 131 (1998).

[27]E. A. Paisley, B. E. Gaddy, J. M. LeBeau, C. T. Shelton, M. D. Biegalski, H. M. Christen, M. D. Losego, S. Mita, R. Collazo, Z. Sitar, D. L. Irving, and J.-P. Maria, J. Appl. Phys. **115**, 064101 (2014).

[28]E. D. Grimley, "Quantification of atomic-scale structuring and polar phenomena in oxides and nitrides," Ph.D. thesis (North Carolina State University, 2018).

[29]C. Martínez-Boubeta, A. S. Botana, V. Pardo, D. Baldomir, A. Antony, J. Bertomeu, J. M. Rebled, L. López-Conesa, S. Estradé, and F. Peiró, Phys. Rev. B **86**, 041407(R) (2012).

[30]H. Goto, S. W. Lee, H. J. Lee, H.-J. Lee, J. S. Ha, M. W. Cho, and T. Yao, Phys. Status Solidi C **5**, 1659 (2008).